



OPEN High efficiency focusing vortex generation and multichannel multiplexing based on terahertz metasurfaces

Wenyu Li^{1,2,3}, Tianhua Meng^{1,3}, Lijuan Dong^{1,3}, Lixiang Liu^{1,3}, Jingyu Liu² & Guozhong Zhao²✉

Single-function metasurfaces can only perform one task and thus cannot satisfy the demands of many advanced applications. Employing multifunctional and multiplexing metasurfaces considerably increases the integration density of functional devices. Therefore, orbital angular momentum (OAM) multiplexing metasurfaces have been designed to increase transmission capacity. In this study, a bilayer Pancharatnam–Berry phase unit cell operating at two frequencies in the terahertz (THz) band is proposed. The unit cell has a sub-wavelength thickness that can be used as a functional element for constructing ultrathin and compact metasurfaces for wavefront manipulation. Cross-polarization conversion ratio of 86.3% and 88.5% are obtained at the two frequencies, respectively. We design three multifunction metasurfaces to verify the method. First, two vortex metalenses are designed to focus vortex beams in the sub-wavelength scale at various frequencies. Furthermore, multichannel OAMs with various modes and arbitrary shape of OAM beam arrays can be realized using segmented metasurfaces. Finally, multichannel OAM multiplexing with the frequency selection and polarization dependence were simultaneously realized on a metasurface. Such metasurfaces can be used to realize large-capacity and high-spectrum-efficiency OAM communication. This paper contributes to the disciplines of photonic integration, multiplexing, and multifunctional metasurfaces.

Keywords Metasurface, Terahertz (THz), Orbital angular momentum (OAM) multiplexing

In addition to linear momentum, electromagnetic waves exhibit angular momentum, including spin angular momentum and orbital angular momentum (OAM). The OAM mode number can be infinite and the beams with different mode numbers are orthogonal. OAM beams have been applied in modern optical communications because OAM provides a new degree of freedom and increases data capacity^{1,2}. Conventional OAM beam generators are bulky and difficult to integrate. For a single-mode OAM generator, only a certain mode of vortex beam can be generated at a given time³. Furthermore, the vortex beams should be focused at a certain position to avoid divergence caused by the transmission process, which requires an additional lens in the optical path. Thus, the optical communication system becomes complex and has lower integration density^{4,5}. Metasurfaces have attracted considerable research attention because of their ultrathin and dense structure as well as their ability to manipulate electromagnetic waves^{6–9}. Superimposing different metasurfaces can result in beams with complicated features^{10,11}.

Although considerable achievements have been realized in obtaining customized single functions using metasurfaces, single-channel vortex beam generators can no longer satisfy the urgent requirements of large data storage capacity demanded in current applications. Therefore, studies have focused on designing metasurfaces that can handle multiple tasks concurrently^{12,13}. With the development of multiplexed communication technologies, ultrathin and multifunctional metasurfaces have received considerable attention, which have opened novel avenues for achieving high-density functionality and effectively reducing the size of photonic systems^{13–16}. Through segmented, interleaved, few-layer designs of unit cells, various information can be multiplexed into distinct channels for integrating various functions^{12,17}. Generally, multiplexing refers to optical communication consisting of various information channels for integrating various channels into a single metasurface^{18–24}. For

¹Institute of Solid State Physics, Shanxi Datong University, Datong 037009, China. ²Department of Physics, Capital Normal University, Beijing Key Lab for THz Spectroscopy and Imaging, Key Lab of THz Optoelectronics, Ministry of Education, Beijing 100048, China. ³Shanxi Provincial Key Laboratory of Microstructure Electromagnetic Functional Materials, Shanxi Datong University, Datong 037009, China. ✉email: guozhong-zhao@cnu.edu.cn

example, Mehmood et al.⁴ designed high-concentration focused vortex beams with different mode numbers on different longitudinal focal planes. Li et al.¹⁶ and Zhao et al.¹⁸ proposed OAM multiplexing and demultiplexing with a single metasurface in the visible and terahertz (THz) wavebands, respectively. Ding et al.¹⁹ reported a dual-focal metasurface and achieved a Gaussian-distributed intensity and a focused vortex beam at two focal points in the same plane. In addition to the above-mentioned metal metasurfaces for implementing OAM multiplexing, Li et al.²¹ used a dielectric metasurface to achieve a ten-channel efficient angular momentum multiplexing and demultiplexing. The spatial dimension resources of optical waves can be used in multiplexing technologies, such as wavelength division multiplexing (WDM), polarization division multiplexing (PDM), and space division multiplexing (SDM)^{12,16}. The development of multidimensional resources of optical wave provides a novel approach for the sustainable expansion of optical communication. To achieve higher communication rates, OAM multiplexing is typically combined with WDM, PDM, and SDM. Thus, numerous breakthroughs have been achieved in the number of OAM multiplexed channels, spectral efficiency and transmission capacity of the system constantly^{16,24}. However, limited studies have focused on multichannel OAM multiplexing with frequency-selective polarization-dependent metasurfaces. Designing specific optical functions at various frequencies is a fundamental requirement for the development of integrated photonics and crucial for improving system capacity and spectrum efficiency¹². By exploiting multiple degrees of freedom, metasurfaces could theoretically carry more efficient functions and exhibit tighter integration.

In this study, a high-efficiency unit cell is designed at two frequencies in the THz band. Two vortex metasurfaces are achieved at different frequencies by combining the focus and the helical phases. multichannel OAMs with distinct modes and arbitrary shape of vortex beams arrays can be realized using segmented metasurfaces. An ultrathin and compact metasurface, which is constructed through segmented design using the dual-frequency response of unit cells, is used to achieve multichannel OAM multiplexing with frequency-selective and polarization dependent characteristics. This method greatly improves the integration density of metasurface functional devices as well as multiplexing efficiency of the device.

Results and discussion

Theoretical analysis and design of the unit cell

First, a unit cell, with dual-frequency operation as well as high cross-polarized transmittance should be designed to obtain a dual-frequency and high-efficiency THz metasurface device. The conditions that high-performance unit cell should satisfy are first designed. For the unit cell rotating at an angle of α with a plane circularly polarized (CP) wave incidence, the Jones matrix was used to obtain the expressions of the co-polarized and cross-polarized transmission coefficients and demonstrate the condition when the cross-polarized transmission coefficients reached 1²⁵. First, the matrix of the CP transmission coefficient can be expressed as follows:

$$T_{\text{cir}}(\alpha) = \sigma^{-1} T(\alpha) \sigma = \begin{bmatrix} t_{LL} & t_{LR} \\ t_{RL} & t_{RR} \end{bmatrix} \quad (1)$$

where subscripts L and R refer to left-handed circularly polarized (LCP) and right-handed circularly polarized (RCP), respectively. Here, t_{LR} expresses the transmission coefficient for the beam of LCP by RCP illumination, others have the same definition. Next, $\sigma = \frac{1}{\sqrt{2}} \begin{bmatrix} 1 & 1 \\ i & -i \end{bmatrix}$ represents the transformation matrix, which converts the linearly polarized transmission matrix to the CP matrix. Furthermore, $T(\alpha)$ is the transmission matrix when the unit cell rotates by an angle of α and is expressed as follows:

$$T(\alpha) = M^{-1}(\alpha) TM(\alpha) = \begin{bmatrix} \cos(\alpha) & -\sin(\alpha) \\ \sin(\alpha) & \cos(\alpha) \end{bmatrix} \begin{bmatrix} t_{xx} & t_{xy} \\ t_{yx} & t_{yy} \end{bmatrix} \begin{bmatrix} \cos(\alpha) & \sin(\alpha) \\ -\sin(\alpha) & \cos(\alpha) \end{bmatrix} \quad (2)$$

Therefore, the co-polarized and cross-polarized transmission coefficients can be represented as follows:

$$t_{LL} = \frac{1}{2} [(t_{xx} + t_{yy}) + i \cdot (t_{xy} - t_{yx})] \quad (3a)$$

$$t_{LR} = \frac{1}{2} [(t_{xx} - t_{yy}) - i \cdot (t_{xy} + t_{yx})] \cdot e^{i \cdot 2\alpha} \quad (3b)$$

$$t_{RL} = \frac{1}{2} [(t_{xx} - t_{yy}) + i \cdot (t_{xy} + t_{yx})] \cdot e^{-i \cdot 2\alpha} \quad (3c)$$

$$t_{RR} = \frac{1}{2} [(t_{xx} + t_{yy}) - i \cdot (t_{xy} - t_{yx})] \quad (3d)$$

where t_{xx} , t_{yy} , t_{xy} , and t_{yx} are co-polarized and cross-polarized transmission coefficients in the linear polarization base. Equations (3a) and (3d) reveal that the co-polarized component is not affected by the rotation angle α of the unit cell, that is, the phase of the co-polarization remains unchanged with the change in the rotating angle. However, Eqs. (3b) and (3c) reveal that the cross-polarized component introduces a phase change of $\pm 2\alpha$, which is the Pancharatnam-Berry (P-B) phase, the plus or minus sign is related to the polarization state of the incident CP wave^{26,27}. In theory, when $t_{xx} + t_{yy} = 0$ and $t_{xy} - t_{yx} = 0$ are satisfied at the same time, the co-polarized component disappears under CP incidence, only the cross-polarized term is preserved²⁸. As reported in previous literatures, two methods, namely half-wave plate^{29,30} and quarter-wave plate²⁵, satisfy the aforementioned conditions. Both these methods can effectively improve cross-polarization transmittance by reducing co-polarization transmission. To achieve a high cross-polarization transmittance base on half-wave

plate, the co-polarized components in linear polarization base should have equal magnitudes and a π -phase retardation, $t_{xx} = -t_{yy}$, and the cross-polarized components vanish, $t_{xy} = t_{yx} = 0$. However, because of some unavoidable losses, the actual efficiency of 100% cannot be achieved^{25,31}. Many unit cells based on the aforementioned two methods are single-frequency operations^{25,28–31}. Therefore, dual-frequency operation should be realized for achieving high polarization conversion efficiency in the transmission.

The bilayer structure can be used to achieve high transmittance and π -phase difference between the co-transmission coefficients in the linear polarization base³². A bilayer unit cell, composed of two identical metal resonator elements and a middle dielectric layer, is designed in the THz band. The top and side views of the proposed unit cell are displayed in the right inset of Fig. 1a. The metallic pattern consists of a square double split ring and a middle strip, which can be regarded as an integral structure composed of two rectangle split ring resonators back to back. The two layers of the metallic pattern exhibit exactly the same geometry. The period of the unit cell is $p = 100 \mu\text{m}$, the thickness of metal layers on the top and bottom layers is $t_1 = 0.2 \mu\text{m}$. The remaining structural parameters are as follows: $a = 70 \mu\text{m}$, $l = 18 \mu\text{m}$, $w = 10 \mu\text{m}$, and α is the rotation angle of the unit cell. The dielectric spacer is a 30- μm -thick polyimide with a relative permittivity of $\epsilon_r = 3.5$ and a loss tangent of 0.0027. The CST Microwave Studio was used to optimize and stimulate the geometry parameters and the electromagnetic properties of the unit cell. In the simulation, the unit cell boundary conditions were applied in both x - and y -directions, and open boundary conditions were used in the z -direction. The incident wave was vertical incidence from the $+z$ direction along the $-z$ direction. The amplitude and phase of the transmission coefficients versus the frequency with linearly polarized wave incidence are plotted in Fig. 1b, c. The amplitudes of both t_{xx} and t_{yy} are equal and close to 0.9 at two frequencies ($\nu_1 = 0.83\text{THz}$, $\lambda_1 = 361\mu\text{m}$, $\nu_2 = 1.72\text{THz}$, and $\lambda_2 = 174\mu\text{m}$). The cross-polarized transmission coefficients t_{xy} and t_{yx} are almost zero because of mirror symmetry of the unit cell about the xz and yz planes. However, the phase difference is not strictly π at two operating frequencies, as displayed in Fig. 1c. According to the previous analyses, this result leads to an imperfect half-wave plate at the two frequencies, and the cross-polarized transmission cannot reach 1. When the LCP wave is incident normally, the cross-polarized transmission coefficient is displayed in Fig. 1d. Notably, the cross-polarized transmission amplitude reached its maximum of 0.85 at 0.83 and 1.72 THz. The polarization conversion ratio (PCR) is defined as $\text{PCR} = t_{RL}^2/t_{RL}^2 + t_{LL}^2$ and used to denote the proportion of cross-polarized components in the transmitted wave^{19,27}. Figure 1e, f display co-polarized transmittance T_{LL} , cross-polarized transmittance T_{RL} , PCR and cross-polarized transmission phase changes φ_{RL} of the unit cells with various rotation angles under LCP incidence normally at 0.83 and 1.72 THz. T_{LL} and T_{RL} are the transmittance and are the square of the transmission coefficient. Notably, T_{RL} is considerably higher than T_{LL} , with an average value of 70.3% and 67.1% at the two frequencies, respectively. The simulated average PCR is 86.3% and 88.5% at 0.83 and 1.72 THz, respectively. The cross-polarized component occupies most of the energy in the transmitted beam, and only a small part of co-polarized components can pass through the metasurface as a negligible background energy at two frequencies. When the polarization state of the incident beam is changed from LCP to RCP, the sign of the phase shift also changes because such a P-B phase has polarization dependence. Moreover, the arbitrary phase shift φ between 0 and 2π can be achieved by simply changing the rotating angle of the unit cell. Crucially, such a unit cell can easily control the phase change at the two frequencies with a high PCR. Unlike other studies^{33–35}, a combination of two resonators with distinct operating wavelengths were used, and the two resonators were adjusted separately to achieve dual-wavelength operation. However, this technique is considerably more complex than the design proposed in this study. The transmittance maintains slight fluctuations, and the arbitrary phase shift at the two wavelengths were adjusted simultaneously by simply rotating the direction of the unit cell. The following simulation results confirmed that the mutual interference of these two frequencies was weak. Furthermore, the total thickness of the unit cell is lower than $\lambda_1/12$ ($\lambda_1 = 361 \mu\text{m}$) and $\lambda_2/6$ ($\lambda_2 = 174 \mu\text{m}$) at two operating frequencies. The deigned bilayer unit cell could be used as the functional elements of potential applications in frequency selection, polarization dependence, high efficiency, and compact integrated optical systems.

The physical mechanism of the bilayer unit cell at two frequencies of 0.83 and 1.72 THz were investigated by evaluating the surface current distributions on both top and bottom metal layers displayed in Fig. 2. At 0.83 THz, for the x-linear polarized (XLP) wave incident normally, the opposite electric dipole oscillations were excited on top and bottom metal layers, respectively, as displayed in Fig. 2a, b, to form a ring current. Therefore, the magnetic dipole was excited in the dielectric layer, which is the parallel to the direction of the magnetic field component of the incident wave. A strong magnetic response with the incident wave was produced. For the y-linear-polarized (YLP) wave incident normally, the polarization direction of electric field of the incident electromagnetic wave was parallel to the opening direction of the double split rings, the free electrons in the metal conductor at the gap were redistributed, and the induced charges generated by the incident electric field were distributed at the gap to form a capacitor structure. Meanwhile, the induced charges moved in the ring, forming a circular current, thus can generate a magnetic field. The arm of ring is equivalent to the inductance to store magnetic energy. Hence, the split ring can be thought as an LC oscillation circuit, and the capacitance of the split gap battles the self-inductance of each loop to generate the resonance^{36,37}. As can be seen from the surface current distributions in Fig. 2c, d, an LC resonance was generated in the left and right split rings on top and bottom metal layers, respectively. The LC resonance frequency is calculated by

$$f = \frac{1}{2\pi\sqrt{LC}} \quad (4)$$

where, L is the equivalent inductance, proportional to the geometric area of the incident field across the split-ring resonator³⁸. C is the equivalent capacitance of the split gap, and it can be thought as a parallel-plate capacitor, the capacitance is

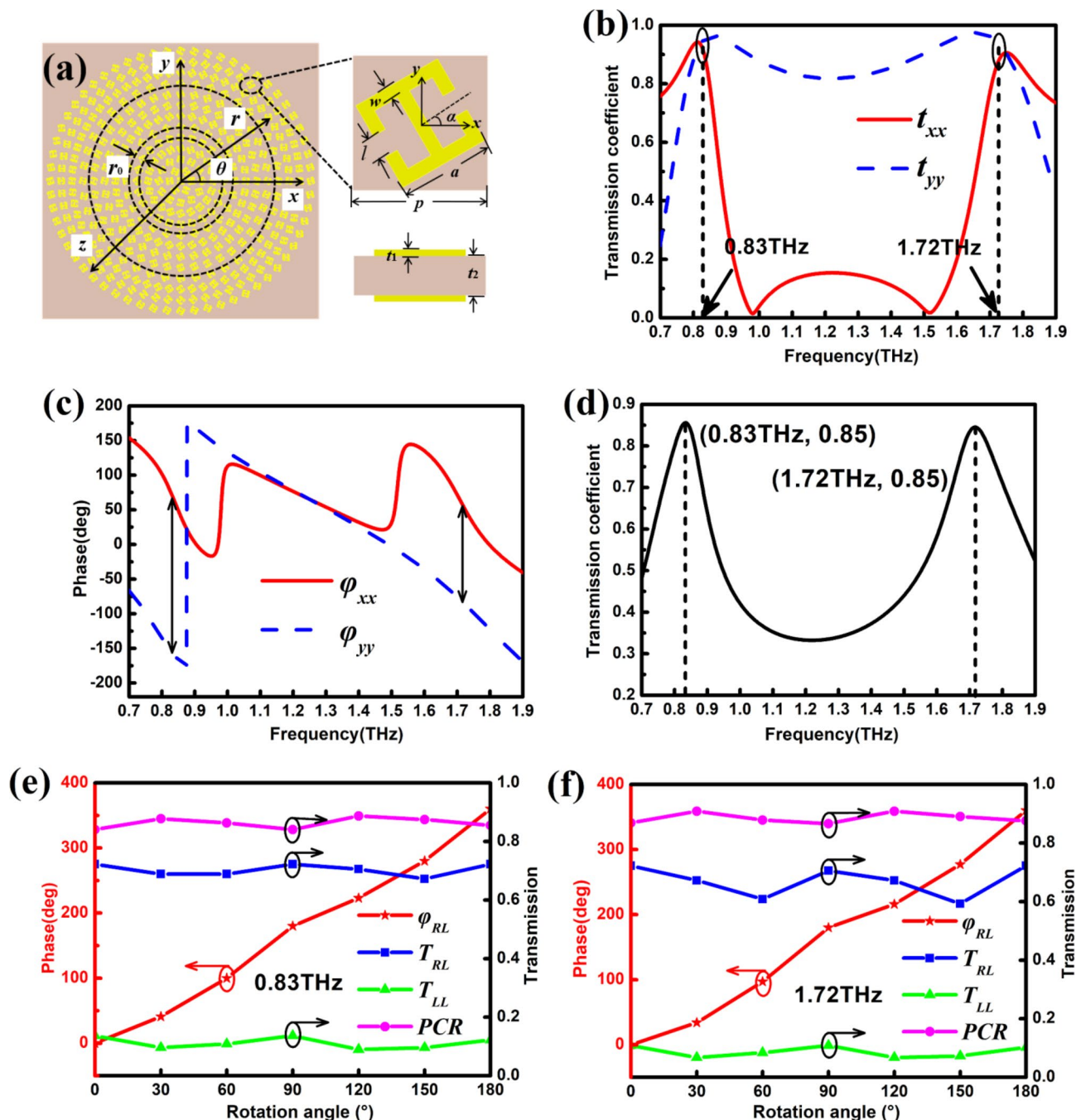


Fig. 1. (a) Schematic of the designed vortex metasurface. All unit cells were arranged in concentric circles. The inset displays top and side views of the unit cell. Simulated transmission magnitudes (b) and phase spectra (c) of the designed unit cell under various linear polarized incidence. (d) The cross-polarized transmission magnitudes illuminated by the normally incident LCP wave. Simulated co-polarized transmittance T_{LL} , cross-polarized transmittance T_{RL} , PCR and cross-polarized transmission phase changes φ_{RL} of the unit cells with various rotation angles under LCP incidence normally at 0.83 THz (e) and 1.72 THz (f).

$$C = \frac{\varepsilon_0 S}{4\pi k d} \quad (5)$$

where S is the corresponding area of gap, d is the width of gap, and k is electrostatic constant. Although the magnetic dipole could be generated by LC resonance, its direction is the same as the propagation direction of the incident electromagnetic wave and is orthogonal to the magnetic field component. Therefore, the magnetic response is weak. At 0.83 THz, magnetic resonances were excited in the bilayer unit cell in addition to the electric resonances under XLP (YLP) incidence. However, at 1.72 THz, for XLP wave incidence, electric dipole

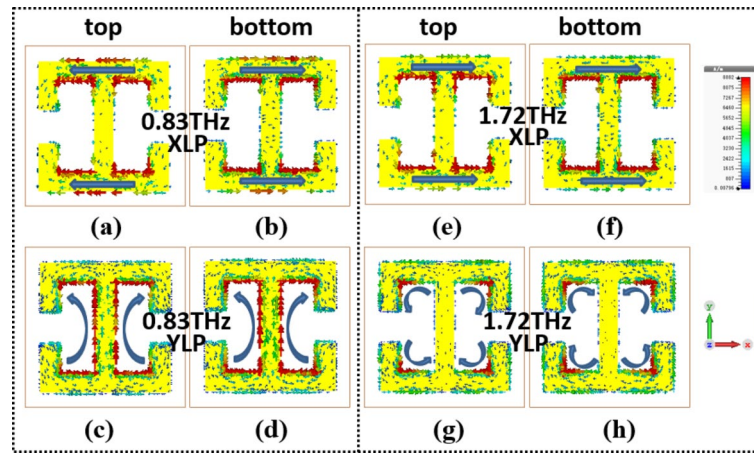


Fig. 2. Surface current distributions at 0.83 THz. (a) Top and (b) bottom layers of the unit cell under XLP incidence. (c) Top and (d) bottom layers of the unit cell under YLP incidence. The surface current distributions at 1.72 THz. (e) Top and (f) bottom layers of the unit cell under XLP incidence. (g) Top and (h) bottom layers of the unit cell under YLP incidence.

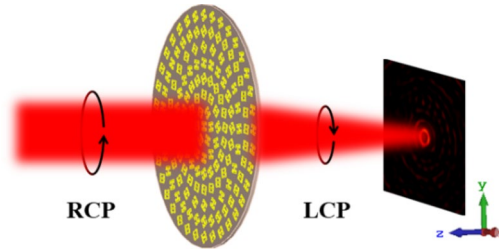


Fig. 3. Schematic illustration of a metasurface for cross-polarization conversion and focused vortex beam generation under RCP illumination along the negative z -axis.

oscillations with the same direction were generated on the top and bottom metal layers of the unit cell in Fig. 2e, f. Distinguish surface current distributions in Fig. 2c, d, for the YLP wave incidence, four pair electric dipole resonances were distributed on the upper and lower sides of two rectangle split ring resonators in two metal layers in Fig. 2g, h, respectively. Therefore, at 1.72 THz, electrical resonances typically occur in the unit cell. In short, we design a metal resonator element by using two rectangle split ring resonators back to back, and construct a bilayer unit cell with two identical resonator elements designed. The bilayer unit cell can support various resonant modes to realize dual-frequency operation. The interaction between the double-layer metal resonator elements can further improve the cross-polarized transmittance at these two frequencies. In addition, the arbitrary phase shift can be achieved at both operating frequencies by changing the rotating angle of the unit cell, which greatly simplifies the difficulty of constructing dual-frequency efficient terahertz metasurface devices. At the same time, this design idea can also be applied to the design of dual-frequency high-efficiency devices in other frequency bands.

Generation of the focused vortex beam

Figure 3 illustrates the process of the metasurface for cross-polarization conversion and focused vortex beam generation under RCP illumination along the negative z -axis. The metasurface used in Fig. 3 is not 12 concentric rings, but only shows the central part of the designed concentric rings. To convert the incident CP plane wave into a focused vortex wave carrying OAM, two phase distributions should be satisfied, namely the spiral phase distribution along the azimuth direction and the focus phase distribution along the radial direction. By superposing the spiral phase and focus phase, the phase distribution of metasurface can be expressed in polar coordinates as follows³⁹:

$$\varphi(r, \theta) = \pm \frac{2\pi}{\lambda} \left(f - \sqrt{r^2 + f^2} \right) + l \cdot \theta \quad (6)$$

Where λ is the wavelength in the free space, f is the focal length of metasurface, l represents the topological charge of OAM, r is the distance from the coordinate origin, and θ is the azimuthal angle. Because of the phase change of the P-B element depends on the rotation angle α of the unit cell and the addition phase delay is twice of α . Therefore, the rotation angle α of the unit cell can be expressed as follows:

$$\alpha(r, \theta) = \pm \frac{\pi}{\lambda} \left(f - \sqrt{r^2 + f^2} \right) + \frac{1}{2} l \cdot \theta \quad (7)$$

Based on the aforementioned analysis, two vortex metasurfaces are constructed by properly arranging unit cells with the rotation angle of α . According to formula (7), a vortex metasurface that operates at a frequency of 0.83 THz ($\lambda_1 = 361 \mu\text{m}$) is designed as displayed in Fig. 1a. Centered at the origin of coordinates, the 12 concentric ring of arrays are arranged. The focal length is designed to be 900 μm , the topological charge l is 1, and r represents the distance from unit cell to the origin of the coordinate, that is, $r = i \cdot r_0$ (i represents the number of turns of the unit cell). The distance between every two circles is $r_0 = 120 \mu\text{m}$. Considering the factors of non-overlapping between each unit cell and the difficulty of processing, the values of the angle between the adjacent unit cells in each circle and the origin of the coordinate are set as follows: 60°, 30°, 18°, 15°, 15°, 10°, 10°, 9°, 9°, 6° and 6°. The numbers of unit cells in each circle are 6, 12, 20, 24, 24, 36, 36, 40, 40, 60, 60 and 60. The dimension of metasurface is 3050 $\mu\text{m} \times 3050 \mu\text{m}$. In the simulation, RCP Gaussian beam illuminates the metasurface normally along the negative z -axis. The frequency of Gaussian beam is set to the operating frequency, the focal spot is located in the center of the entire metasurface. The waist radius is set to 2200 μm , so the beam could be uniformly incident on the entire metasurface. The open boundary conditions are used in x , y and z directions. An electric field monitor, which is 3000 $\mu\text{m} \times 3000 \mu\text{m}$, is placed 900 μm behind the metasurface, and another electric field monitor, which is 4000 $\mu\text{m} \times 4000 \mu\text{m}$, is placed at $Y=0$ to observe the focusing of the beam in the propagation path. The simulation settings above also apply to the simulation process of metasurfaces mentioned below. The simulated longitudinal and transverse cross-polarized electric field intensity distributions are displayed in Fig. 4a, b. The longitudinal distribution diagram reveals that the transmitted LCP electric field is concentrated in the compact area around z -axis, with dark spots in the middle and bright spots on both sides. The white dotted line indicates the position of the focal plane. The energy is typically concentrated near the focal plane, with obvious focusing effect and no divergence. Figure 4b displays the cross-sectional distribution of the electric field intensity at the focal plane of $z=900 \mu\text{m}$. The intensity distribution is a circular ring with a dark spot in the center, which is a direct result of the optical vortex. The inset of Fig. 4b displays the phase distribution diagram, the spiral pattern can be clearly observed, and the phase change of one rotation around the center is 2π , which indicates that the topological charge of the generated OAM wave is 1. Figure 4c details the corresponding normalized intensity spectra along the x -axis at the focal plane. The full-wave half maximum (FWHM) at the focal plane is used to describe the size and imaging quality of the focal spot of the lens. Generally, the smaller FWHM is, the more concentrated the energy is^{2,40}. The FWHM of the donut-shaped spot is 226 μm (0.63 λ_1). The vortex metasurface designed can effectively generate a focused vortex beam with OAM. Another vortex metasurface that operates at a frequency of 1.72 THz ($\lambda_2 = 174 \mu\text{m}$) is designed, and the simulated longitudinal

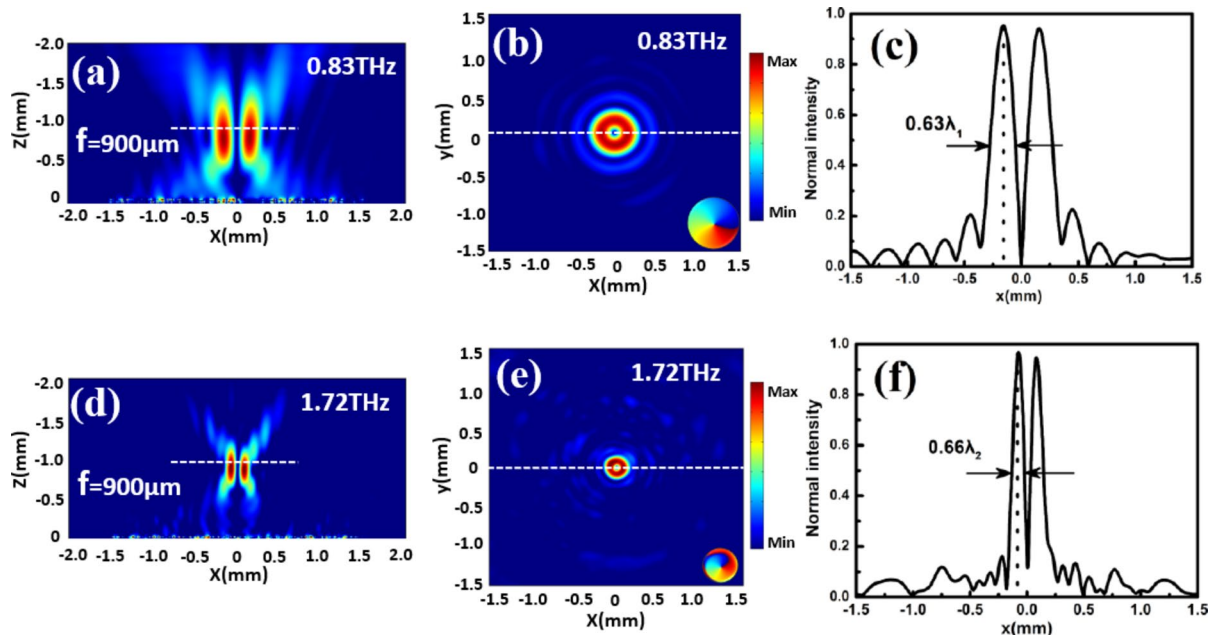


Fig. 4. Simulated electric field distributions of the generated focused vortex beam for topological charge $l=1$ at 0.83 THz. (a) Energy intensity of the longitudinal electric field of the converted OAM beam with $l=1$ in the xoz plane. (b) Energy intensity of the electric field in the xoy plane at $z=-900 \mu\text{m}$. (c) The normalized electric field intensity spectra of focused vortex beam along the x -axis at the focal plane of $z=-900 \mu\text{m}$. Simulated electric field distributions of the generated focused vortex beam for topological charge $l=1$ at 1.72 THz. (d) The energy intensity of the longitudinal electric field of converted OAM beam with $l=1$ in the xoz plane. (e) The energy intensity of the electric field in the xoy plane at $z=-900 \mu\text{m}$. (f) The normalized electric field intensity spectra of the focused vortex beam along the x -axis in the xoy plane at the focal plane of $z=-900 \mu\text{m}$.

and transverse cross-polarized electric field intensity distributions are displayed in Fig. 4d, e. The FWHM of normalized intensity spectra of the donut-shaped spot is $114 \mu\text{m}$ ($0.66 \lambda_2$), as displayed in Fig. 4f. The designed metalens can generate a focused vortex beam with the sub-wavelength scale, which can concentrate the incident energy and effectively increase the utilization efficiency of the vortex beam. This phenomenon is expected to be realized in most optical applications. The phase change at two frequencies can be effectively regulated by using the rotating unit cell. By arranging units with various rotation angles at different positions, the two focused vortex lenses can focus the transmitted cross-polarized beam at the position of the focal plane, and carry the angular spiral phase.

Multichannel OAM generator with segmented metasurfaces

Although the designed single-channel vortex beam generator achieves excellent focusing at a specific location and carries OAM, only a vortex beam with a topological charge is generated at a single frequency each time. With the development of multiplexing communication technology, a single design can no longer satisfy the urgent requirements of large data storage capacity. Simultaneous generation of OAM beams with various mode numbers under a single illumination from a metasurface has received considerable research attention^{15,41}. In this section, the generation of multichannel focused vortex beams on a metasurface using a segmented design was detailed. For the segmented design, each channel generates from a different area of the device. Each part is independent from other parts and does not affect the other. This phenomenon renders the design easy to implement with limited mutual interference. The design scheme is as follows: considering the origin of coordinates as the center, the entire metasurface is divided into four parts according to four quadrants. As displayed in Fig. 5a, each part takes (x_0, y_0) , $(-x_0, y_0)$, $(-x_0, -y_0)$, and $(x_0, -y_0)$ as the origin of the four quadrants to establish four temporary coordinate systems (r_i, θ_i) , $i = 1, 2, 3, 4$, $x_0 = 0.75 \text{ mm}$, $y_0 = 0.75 \text{ mm}$. The dimension of the segmented metasurface is $2900 \mu\text{m} \times 2900 \mu\text{m}$. Centered at the origins of the four temporary coordinates, five concentric ring functional element of arrays were arranged in each section to generate focused OAM beams with various topological charges $(1, 0, -1, 2)$ at the focal plane according to the following equation:

$$\alpha(r_1, \theta_1) = \frac{\pi}{\lambda_2} \left(f_1 - \sqrt{r_1^2 + f_1^2} \right) + \frac{1}{2}\theta_1, \quad 0 < \theta \leq \frac{\pi}{2} \quad (8a)$$

$$\alpha(r_2, \theta_2) = \frac{\pi}{\lambda_2} \left(f_1 - \sqrt{r_2^2 + f_1^2} \right), \quad \frac{\pi}{2} < \theta \leq \pi \quad (8b)$$

$$\alpha(r_3, \theta_3) = \frac{\pi}{\lambda_2} \left(f_1 - \sqrt{r_3^2 + f_1^2} \right) - \frac{1}{2}\theta_3, \quad \pi < \theta \leq \frac{3\pi}{2} \quad (8c)$$

$$\alpha(r_4, \theta_4) = \frac{\pi}{\lambda_2} \left(f_1 - \sqrt{r_4^2 + f_1^2} \right) + \theta_4, \quad \frac{3\pi}{2} < \theta \leq 2\pi \quad (8d)$$

where $f_1 = 500 \mu\text{m}$, is the focal length from the metasurface to the focal plane, $\lambda_2 = 174 \mu\text{m}$ ($\nu_2 = 1.72 \text{ THz}$). When vertical irradiation of the RCP Gaussian beam on the metasurface at 1.72 THz , the simulated cross-polarized intensity distribution of the multichannel OAM generator at the focal plane are displayed in Fig. 5b. Transmitted cross-polarized beam forms various focal spots, including a solid spot and three donut spots, on the focal plane $500 \mu\text{m}$ away from the metasurface. The insets in Fig. 5b are the phase distributions of the three focused vortices, respectively. According to the phase distribution diagrams, the topological charges are $1, -1$, and 2 , respectively. The topological charge of the vortex beam increases from 1 to 2 , and the corresponding focal spot expands. The ring radius of the vortex intensity distribution increases, but the annular shape remains unchanged because the phase singularity of the center point increases with the increase in the topological charge number, which leads to the appearance of large dark spot. However, all four foci are well separated from each other. The distance between two adjacent foci was set to $1500 \mu\text{m}$, and the FWHM of the foci was considerably less than this distance. Therefore, the distinction between each foci is obvious. Because of the interference between

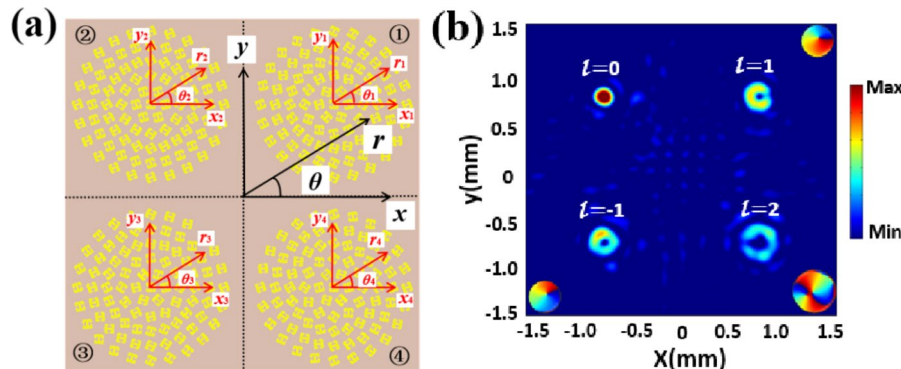


Fig. 5. (a) Top view of the segmented metasurface used to generate multichannel OAM beams with various topological charges. (b) Intensity profiles of the multichannel segmented metasurface under RCP irradiation at 1.72 THz .

segmented regions, some interactions exist between adjacent functional areas. However, the interactions are weak and are negligible compared with the main foci. The spacing between adjacent functional areas is 200 μm . The interactions can be reduced by increasing the distance between the regions. A larger interval results in a weaker cross-talk. However, this interval was selected for the compactness of the design metasurface. Therefore, the metasurface can realize multi-focus and multi-vortex spatial multiplexing. More channels and higher OAM multiplexing can be generated by larger segmented metasurfaces.

Furthermore, the segmented metasurface can easily generate multi-focal vortex arrays of arbitrary shapes. According to the same design method, the metasurface in Fig. 6a is categorized into five parts centered at the origin. The polar coordinates (r, θ) are established with the y-axis as the polar axis. The five parts take (1500 μm , 0°), (1500 μm , 72°), (1500 μm , 144°), (1500 μm , 216°) and (1500 μm , 288°) as the origins to establish five temporary coordinate systems (r_i, θ_i) , $i=1, 2, 3, 4, 5$, and each part is arranged with five concentric ring functional elements of arrays according to Eq. (8a). The dimension of the segmented metasurface is 4350 $\mu\text{m} \times 4350 \mu\text{m}$. Figure 6b displays a multichannel vortex beams ($l=1$) with pentagonal array distribution. An arbitrary shape vortex beam array with distinct channels and different topological charges can be designed as per requirement. Such vortex arrays are highly desired in applications requiring trapping and manipulation of nanoparticles. The same function can also be designed using the same method and implemented at 0.83 THz.

OAM multiplexing with frequency selection and polarization dependence

Apart from multichannel OAM generation, arbitrary control of various incident polarizations and frequencies using a metasurface with an ultrathin and compact planar structure is crucial. In this section, the dual-frequency functional elements designed are independently regulated in various areas to achieve multichannel focused vortex beam generation with frequency-selective and polarization-dependent in a compact design. Based on the segmented design, five concentric ring arrays are arranged in each temporary coordinate systems according to the following equation:

$$\alpha(r_1, \theta_1) = \frac{\pi}{\lambda_2} \left(f_1 - \sqrt{r_1^2 + f_1^2} \right) + \frac{1}{2} \theta_1, \quad 0 < \theta \leq \frac{\pi}{2} \quad (9a)$$

$$\alpha(r_2, \theta_2) = \frac{\pi}{\lambda_2} \left(f_1 - \sqrt{r_2^2 + f_1^2} \right), \quad \frac{\pi}{2} < \theta \leq \pi \quad (9b)$$

$$\alpha(r_3, \theta_3) = -\frac{\pi}{\lambda_1} \left(f_1 - \sqrt{r_3^2 + f_1^2} \right) + \frac{1}{2} \theta_3, \quad \pi < \theta \leq \frac{3\pi}{2} \quad (9c)$$

$$\alpha(r_4, \theta_4) = -\frac{\pi}{\lambda_1} \left(f_1 - \sqrt{r_4^2 + f_1^2} \right), \quad \frac{3\pi}{2} < \theta \leq 2\pi \quad (9d)$$

where $f_1 = 500 \mu\text{m}$, and other parameters are defined previously. The segmented metasurface used is identical to that in Fig. 5a in appearance, the arrangement of unit cells differs only in the third and fourth quadrants. The simulation cross-polarized intensity profiles at the focal plane are displayed in Fig. 7a, b. At 0.83 THz, when the LCP is incident normally, a donut focus and a solid focus are generated below the focal plane (Fig. 7a). The phase distribution in the inset reveals that the topological charge is -1 . When the RCP is incident at 1.72 THz, a solid focus, and a hollow focus with a topological charge of 1 are generated above the focal plane (Fig. 7b). When the beams with various frequencies and opposite polarizations are incident normally, interference enhancement occurs at specific locations, and other areas can be regarded as background noise and ignored. Different designed regions of the metasurface respond distinctly to frequencies and polarizations. The simulated results prove that although the phase modulations at the two frequencies are not independent of each other. However, independent manipulation can be achieved at the two frequencies through independent segmental designs.

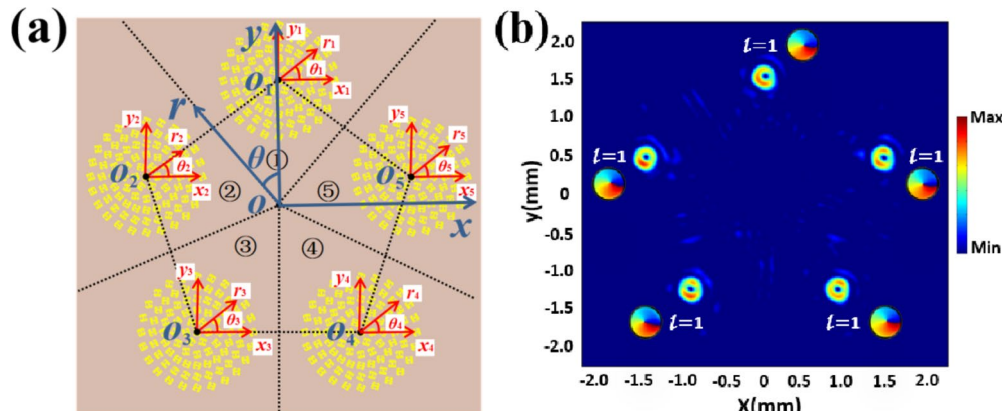


Fig. 6. (a) Top view of the segmented metasurface used to generate multichannel OAM beams with pentagonal array. (b) Intensity profile of multichannel OAM beams with pentagonal array under RCP irradiation at 1.72 THz.

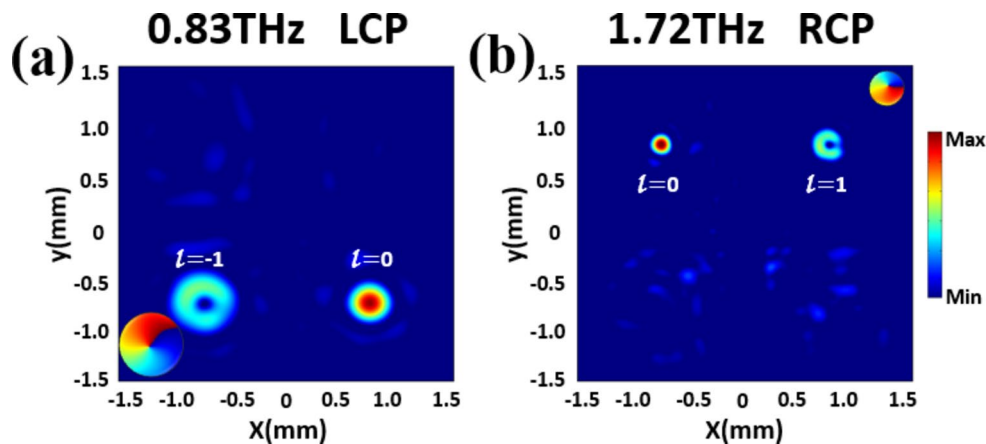


Fig. 7. Intensity profiles of multiplexing metasurface at the focal plane with LCP incidence at 0.83 THz (a) and RCP irradiation at 1.72 THz (b).

The dual-frequency unit cell designed can be used as a functional element to realize dual-frequency response and polarization-dependent multichannel multiplexing metasurfaces using segmented design, in addition to realizing functional devices operating at a single frequency. The multichannel and multiple-degree-of-freedom of multiplexing metasurfaces can satisfy special requirements of frequency-selective, polarization-dependent transmission optics, and integrated photonics.

Conclusion

In summary, a bilayer P–B phase unit cell was constructed by using two rectangle split ring resonators back to back. Due to the generation of different resonances at different frequencies and the interaction between layers, the unit cell can achieve efficient cross-polarized transmittance at two frequencies. Vortex metlenses designed by the principle of phase superposition could focus at the preset focal plane and carry OAM. Then, based on the segmented design method, each region on the metasurfaces is independently regulated, thus realizing the generation of multichannel OAM multiplexing and multichannel vortex with pentagonal array. More importantly, through the customized design of each region, the multi-mode multiplexing of different OAM with dual-frequency and dual-polarization was realized by using a metasurface. These concepts will facilitate the studies of high-capacity optical communication, the trapping and manipulation of nanoparticles, and multifunctional metasurfaces.

Data availability

The datasets used and/or analysed during the current study are available from the corresponding author on reasonable request.

Received: 7 January 2025; Accepted: 20 February 2025

Published online: 03 March 2025

References

1. Bozinovic, N. et al. Terabit-scale orbital angular momentum mode division multiplexing in fibers. *Science* **340**, 1545–1548 (2013).
2. Ou, K. et al. High efficiency focusing vortex generation and detection with polarization-insensitive dielectric metasurfaces. *Nanoscale* **10**, 19154 (2018).
3. Beijersbergen, M. W., Coerwinkel, R. P. C., Kristensen, M. & Woerdman, J. P. Helical-wavefront laser beams produced with a spiral phaseplate. *Opt. Commun.* **112**, 321–327 (1994).
4. Mehmood, M. Q. et al. Visible-frequency metasurface for structuring and spatially multiplexing optical vortices. *Adv. Mater.* **28**, 2533–2539 (2016).
5. Wang, W., Guo, C., Zhao, Z. H., Li, J. & Shi, Y. Polarization multiplexing and bifocal optical vortex Metalens. *Results Phys.* **17**, 103033 (2020).
6. Liu, J. et al. Balanced-ternary-inspired reconfigurable vortex beams using cascaded metasurfaces. *Nanophotonics* **11**, 2369–2379 (2022).
7. Liu, J. P. et al. Generation and detection of broadband multichannel orbital angular momentum by micrometer-scale metareflectorarray. *Opt. Express* **24**, 212–218 (2016).
8. Yu, N. F. et al. Light propagation with phase discontinuities: generalized laws of reflection and refraction. *Science* **334**, 333–337 (2011).
9. Bi, F., Ba, Z. L. & Wang, X. Metasurface-based broadband orbital angular momentum generator in millimeter wave region. *Opt. Express* **26**, 25693–25705 (2018).
10. Zhang, K. et al. Phase-engineered Metalenses to generate converging and non-diffractive vortex beam carrying orbital angular momentum in microwave region. *Opt. Express* **26**, 1351–1360 (2018).
11. Ma, X. L. et al. A planar chiral meta-surface for optical vortex generation and focusing. *Sci. Rep.* **5**, 10365 (2015).
12. Chen, S. Q., Liu, W. W., Li, Z. C., Cheng, H. & Tian, J. G. Metasurface-empowered optical multiplexing and multifunction. *Adv. Mater.* **1805912** (2019).
13. Zhang, C. M. et al. Multichannel metasurface for simultaneous control of holograms and twisted light beams. *ACS Photonics* **4**, 1906–1912 (2017).

14. Wen, D. D. et al. Metasurface device with helicity-dependent functionality. *Adv. Opt. Mater.* **4**, 321–327 (2016).
15. Jin, J. J. et al. Multichannel vortex beam generation by simultaneous amplitude and phase modulation with two-dimensional metamaterial. *Adv. Mater. Technol.* **2**, 1600201 (2016).
16. Li, Y. et al. Orbital angular momentum multiplexing and demultiplexing by a single metasurface. *Adv. Opt. Mater.* **5**, 1600502 (2016).
17. Zhang, D. J. et al. Broadband high-efficiency multiple vortex beams generated by an interleaved geometric-phase multifunctional metasurface. *Opt. Mater. Express.* **10**, 1531–1544 (2020).
18. Zhao, H. et al. Demonstration of orbital angular momentum multiplexing and demultiplexing based on a metasurface in the Terahertz band. *ACS Photonics.* **5**, 1726–1732 (2017).
19. Ding, F., Chen, Y. T. & Bozhevolnyi, S. I. Focused vortex-beam generation using gap-surface plasmon metasurfaces. *Nanophotonics* **9**, 371–378 (2020).
20. Willner, A. E. et al. Optical communications using orbital angular momentum beams. *Adv. Opt. Photonics.* **7**, 66–106 (2015).
21. Li, S. Q. et al. Efficient optical angular momentum manipulation for compact multiplexing and demultiplexing using a dielectric metasurface. *Adv. Opt. Mater.* 1901666 (2020).
22. Zhang, S. et al. Broadband detection of multiple spin and orbital angular momenta via dielectric metasurface. *Laser Photonics Rev.* 2000062 (2020).
23. Ma, Y. B., Rui, G. H., Gu, B. & Cui, Y. P. Trapping and manipulation of nanoparticles using multifocal optical vortex metalens. *Sci. Rep.* **7**, 14611 (2017).
24. Yu, S. X., Li, L. & Shi, G. M. Dual-polarization and dual-mode orbital angular momentum radio vortex beam generated by using reflective metasurface. *Appl. Phys. Express.* **9**, 082202 (2016).
25. Akram, M. R. et al. High efficiency ultrathin transmissive metasurfaces. *Adv. Opt. Mater.* **7**, 1801628 (2019).
26. Karimi, E. et al. Generating optical orbital angular momentum at visible wavelengths using a plasmonic metasurface. *Light-Sci Appl.* **3**, e167 (2014).
27. Li, W. Y., Zhao, G. Z., Meng, T. H., Sun, R. & Guo, J. Y. High efficiency and broad bandwidth Terahertz vortex beam generation based on ultra-thin transmission Pancharatnam-Berry metasurfaces. *Chin. Phys. B.* **30**, 058103 (2020).
28. Tang, S. W. et al. High-efficiency transparent vortex beam generator based on ultrathin Pancharatnam-Berry metasurfaces. *Opt. Express.* **27**, 1816–1824 (2019).
29. Forouzmand, A. et al. Double split-loop resonators as Building blocks of metasurfaces for light manipulation: bending, focusing, and flat-top generation. *J. Opt. Soc. Am. B.* **33**, 1411–1420 (2016).
30. Chen, M. L. N., Jiang, L. J. & Sha, W. E. I. Ultrathin complementary metasurface for orbital angular momentum generation at microwave frequencies. *IEEE T Antenn Propag.* **65**, 396–400 (2017).
31. Luo, W. J., Sun, S. L., Xu, H. X., He, Q. & Zhou, L. Transmissive ultrathin Pancharatnam-Berry metasurfaces with nearly 100% efficiency. *Phys. Rev. Appl.* **7**, 044033 (2017).
32. Zhang, D. et al. Design of single-layer high-efficiency transmitting phase-gradient metasurface and high gain antenna. *J. Phys. D: Appl. Phys.* **50**, 495104 (2017).
33. Liu, K. Y. et al. Dual-frequency geometric phase metasurface for dual-mode vortex beam generator. *J. Phys. D: Appl. Phys.* **52**, 255002 (2019).
34. Ding, J. et al. Dual-wavelength Terahertz metasurfaces with independent phase and amplitude control at each wavelength. *Sci. Rep.* **6**, 34020 (2016).
35. Xie, R. S. et al. High-efficiency ultrathin dual-wavelength Pancharatnam-Berry metasurfaces with complete independent phase control. *Adv. Opt. Mater.* **7**, 1900594 (2019).
36. Linden, S. et al. Magnetic response of metamaterials at 100 Terahertz. *Science* **306**, 1351–1353 (2004).
37. Sun, R., Li, W. Y., Meng, T. H. & Zhao, G. Z. Design and optimization of Terahertz metamaterial sensor with high sensing. *Opt. Commun.* **494**, 127051 (2021).
38. Du, G. H. & Liu, K. Study on characteristics of symmetric split ring resonator for left-handed metamaterial. *J. Sichuan Univ. (Nat Sci. Ed.)* **47**, 1053–1058 (2010).
39. Wang, H. et al. Spatial multiplexing plasmonic Metolenses based on nanometer cross holes. *New. J. Phys.* **20**, 123009 (2018).
40. Ding, J. F. et al. Design and fabrication of off-axis meta-lens with large focal depth. *Acta Phys. Sin.* **70**, 197802 (2021).
41. Maguid, E. et al. Photonic spin-controlled multifunctional shared-aperture antenna array. *Science* **352**, 1202 (2016).

Acknowledgements

This work was supported by the National Natural Science Foundation of China (62071312), the applied basic research projects of Shanxi Province (202403021222262), the Scientific and technological innovation plan project of universities in Shanxi Province (2024L310), the applied basic research projects of Shanxi Province (202203021221212), and the Ph.D. research startup foundation of Shanxi Datong university (2023-B-33).

Author contributions

W.L., T.M., J.L and G.Z. conceived the idea. W.L. designed and simulated the metasurfaces. She also wrote the manuscript. T.M., L.D., L.L., J.L. and G.Z. analyzed the results and revised the draft. G.Z. supervised the whole research work.

Declarations

Competing interests

The authors declare no competing interests.

Additional information

Correspondence and requests for materials should be addressed to G.Z.

Reprints and permissions information is available at www.nature.com/reprints.

Publisher's note Springer Nature remains neutral with regard to jurisdictional claims in published maps and institutional affiliations.

Open Access This article is licensed under a Creative Commons Attribution-NonCommercial-NoDerivatives 4.0 International License, which permits any non-commercial use, sharing, distribution and reproduction in any medium or format, as long as you give appropriate credit to the original author(s) and the source, provide a link to the Creative Commons licence, and indicate if you modified the licensed material. You do not have permission under this licence to share adapted material derived from this article or parts of it. The images or other third party material in this article are included in the article's Creative Commons licence, unless indicated otherwise in a credit line to the material. If material is not included in the article's Creative Commons licence and your intended use is not permitted by statutory regulation or exceeds the permitted use, you will need to obtain permission directly from the copyright holder. To view a copy of this licence, visit <http://creativecommons.org/licenses/by-nc-nd/4.0/>.

© The Author(s) 2025